1
2
# The influence of confining stress and preexisting damage on strain localization in fluid-saturated crystalline rocks in the upper crust

3 **Jessica McBeck[1], Benoît Cordonnier[2], Yehuda Ben-Zion[3], François Renard[1,4]**

4 [1]Njord Centre, Departments of Physics and Geosciences, University of Oslo, Oslo, Norway.

5 [2]European Synchrotron Radiation Facility, Grenoble, France.

6 [3]Department of Earth Sciences and Southern California Earthquake Center, University of
7 Southern California, Los Angeles, CA, USA.

8 [4]Université Grenoble Alpes, Université Savoie Mont Blanc, Université Gustave Eiffel,
9 CNRS, IRD, ISTerre, 38000 Grenoble, France.

10 Corresponding author: Jessica McBeck (j.a.mcbeck@geo.uio.no)

11 **Key Points:**

12 • Digital volume correlation of X-ray tomograms reveals strain localization in triaxial
13   compression experiments.
14 • Larger confining stress promotes localization approaching macroscopic failure.
15 • More preexisting damage promotes episodes of delocalization.

16 **Abstract**

17 The spatial organization of deformation may provide key information about the timing of
18 catastrophic failure in the brittle regime. In an ideal homogenous system, deformation may
19 continually localize toward macroscopic failure, and so increasing localization
20 unambiguously signals approaching failure. However, recent analyses demonstrate that
21 deformation, including low magnitude seismicity, and fractures and strain in triaxial
22 compression experiments, experience temporary phases of delocalization superposed on an
23 overall trend of localization toward large failure events. To constrain the conditions that
24 promote delocalization, we perform a series of X-ray tomography experiments at varying
25 confining stresses (5-20 MPa) and fluid pressures (zero to 10 MPa) on Westerly granite cores
26 with varying amounts of preexisting damage. We track the spatial distribution of the strain
27 events with the highest magnitudes of the population within a given time step. The results
28 show that larger confining stress promotes more dilation, and promotes greater localization of
29 the high strain events approaching macroscopic failure. In contrast, greater amounts of
30 preexisting damage promote delocalization. Importantly, the dilative strain experiences more
31 systematic localization than the shear strain, and so may provide more reliable information
32 about the timing of catastrophic failure than the shear strain.

33 **Plain Language Summary**

34 The ability of deformation, such as fractures and strain, to spatially cluster or localize
35 produces a wide range of geologic features on Earth, such as crustal fault networks and plate
36 tectonics. Previous work demonstrates that deformation can evolve toward more localized
37 distributions. However, recent analyses show that deformation can temporarily decrease in
38 localization. These decreases in localization complicate efforts to use the spatial organization
39 of seismicity, for example, as a precursor of approaching large earthquakes. The factors that
40 promote phases of delocalization remain unconstrained. Here, we perform a series of
41 experiments to identify the factors that control the delocalization of local strain events within
42 low porosity, Westerly granite rock cores. We find that both the confining stress, indicative
43 of depth within the crust, and the amount of preexisting damage of the rock cores control the
44 amount of localization that the strain events experience, and the phases of delocalization.
45 Increasing confining stress produces more localization of the high strain events. More
46 preexisting damage produces more delocalization.

47 **Key words**: localization, strain, triaxial compression, confining stress, dilation, granite

48 **1   Introduction**

49     The localization of strain along fractures, faults, and shear zones is a fundamental
50 phenomenon of rock deformation (e.g., Rudnicki & Rice, 1975; Lockner et al., 1991; Satoh et
51 al., 1996; Benson et al., 2007; Lyakhovsky et al., 2011; Ben-Zion & Zaliapin, 2019). The
52 ability of deformation to localize from the micrometer- to kilometer-scale allowed the Earth's
53 crust to partition into different volumes, and thus is responsible for plate tectonics (e.g.,
54 Gueydan et al., 2014; Mulyukova & Bercovici, 2019). Monitoring the localization of
55 deformation may also be useful for recognizing the development of a preparation phase that
56 leads to catastrophic failure in the upper crust, such as large magnitude earthquakes. In
57 particular, machine learning analyses indicate that tracking the distance between fractures in
58 triaxial compression experiments can help successfully predict the timing of catastrophic
59 failure (McBeck et al., 2020b). Similarly, recent observations show that low magnitude
60 seismicity localized in the final two to three years preceding several *M*>7 earthquakes in
61 Southern and Baja California (Ben-Zion & Zaliapin, 2020). However, for some earthquakes,
62 the seismicity periodically decreased in localization, or delocalized, in the several months

63    preceding the earthquake. These phases of delocalization obscure the relationship between
64    macroscopic failure and localization, and thereby complicate efforts to forecast the timing of
65    an impending large earthquake using the spatial distribution of seismicity. The factors that
66    control whether a rock or crustal volume may experience phases of delocalization remain
67    largely unconstrained.

68    To help constrain these factors, we perform a series of X-ray synchrotron tomography
69    triaxial compression experiments and track the localization of the local three-dimensional
70    strains calculated from digital volume correlation. To assess the influence of confining stress
71    and effective stress on strain localization, we systematically change the confining stress from
72    5 MPa to 20 MPa, and fluid pressure from zero to 10 MPa in the experiments. To assess the
73    influence of preexisting heterogeneities on localization, we introduce a network of
74    preexisting fractures and weaknesses into several of the rock cores by thermal treatment. This
75    set of experiments thus allows comparison of the localization of the strain events in relatively
76    intact and damaged rocks, and in systems with lower and higher confining stress.

## 2   Methods

77
78    2.1. X-ray tomography triaxial compression experiments

79    We performed six triaxial compression experiments at beamline ID19 at the European
80    Synchrotron Radiation Facility. We used 10 mm tall and 4 mm diameter cylinders of
81    Westerly granite, which is a low-porosity crystalline rock dominated by quartz, feldspar, and
82    biotite. The initial porosity is lower than 1%.

83    We imposed a constant confining stress in each experiment (5-20 MPa), and constant
84    pore fluid pressure (0-10 MPa) (**Figure 1**) with the Hades triaxial compression apparatus
85    (Renard et al., 2016). We varied the confining stress and fluid pressure so that five of the
86    experiments experienced the same effective stress, confining stress minus fluid pressure
87    ($P_e$=5 MPa), and one of the experiments experienced $P_e$=10 MPa. **Table** S1 lists all the
88    symbols and notations used here. We increased the axial stress in steps of 0.5-5 MPa until the
89    rock failed with a stress drop, with smaller steps closer to failure. After each increase in axial
90    stress, we acquired a X-ray tomogram within one and half minutes while the core was inside
91    the deformation apparatus.

92    We deformed intact and heat-treated, or damaged, Westerly granite cores. The crack
93    density produced by thermal heating depends on the temperature, differences in the thermal
94    expansion of the minerals, initial porosity, and the grain size (e.g., Fredrich & Wong, 1986).
95    Heating granite to temperatures above 600°C produces significant increases in the crack
96    density and porosity, and decreases in the P-wave speed and uniaxial compressive strength
97    (Griffiths et al., 2017). We heated the cores with an initial heating rate of 4°C/minute from
98    room temperature to 650°C in an oven, and then for five hours at 650°C, and then with a
99    cooling rate of 4°C/minute to room temperature. This heating procedure causes the damaged
100    rock cores to fail at lower differential stresses than the intact rock cores for the same
101    confining stress and effective stress conditions. We performed all the experiments at ambient
102    room temperature in the range 22-24°C. For the experiments that include fluid pressure, we
103    saturated the granite cores in deionized water in a vacuum chamber for two weeks before the
104    experiment.

105    Following each experiment, we reconstructed the acquired radiographs into three-
106    dimensional volumes. The three-dimensional volumes, or tomograms, are 1600x1600x1600
107    voxels, and each voxel side length is 6.5 µm. The spatial resolution of the tomograms is

108    within two to three voxel side lengths. During reconstruction, we applied methods to remove
109    acquisition noise. We then reduced the remaining noise in the reconstructed, three-
110    dimensional data using the software Avizo3D$^{TM}$, such as a non-local means filter (Buades et
111    al., 2005). We calculate the macroscopic axial strain done on the rock cores, $\varepsilon_{zz}$, using the
112    height of the rock core identified in each tomogram. Consequently, the spatial resolution and
113    quality of the tomogram influence the calculated $\varepsilon_{zz}$.

114        In one of the experiments on a damaged core (WG18), a system-spanning, horizontal
115    fracture developed as the core was inserted into the deformation apparatus (**Figure S1**). With
116    increasing axial stress, this fracture closed, and other fractures propagated throughout the
117    core. This large preexisting fracture caused this core to fail at a lower differential stress, and
118    to accumulate more $\varepsilon_{zz}$ preceding macroscopic failure than expected, and than the other
119    experiments. This experiment thus represents an endmember of rock deformation within a
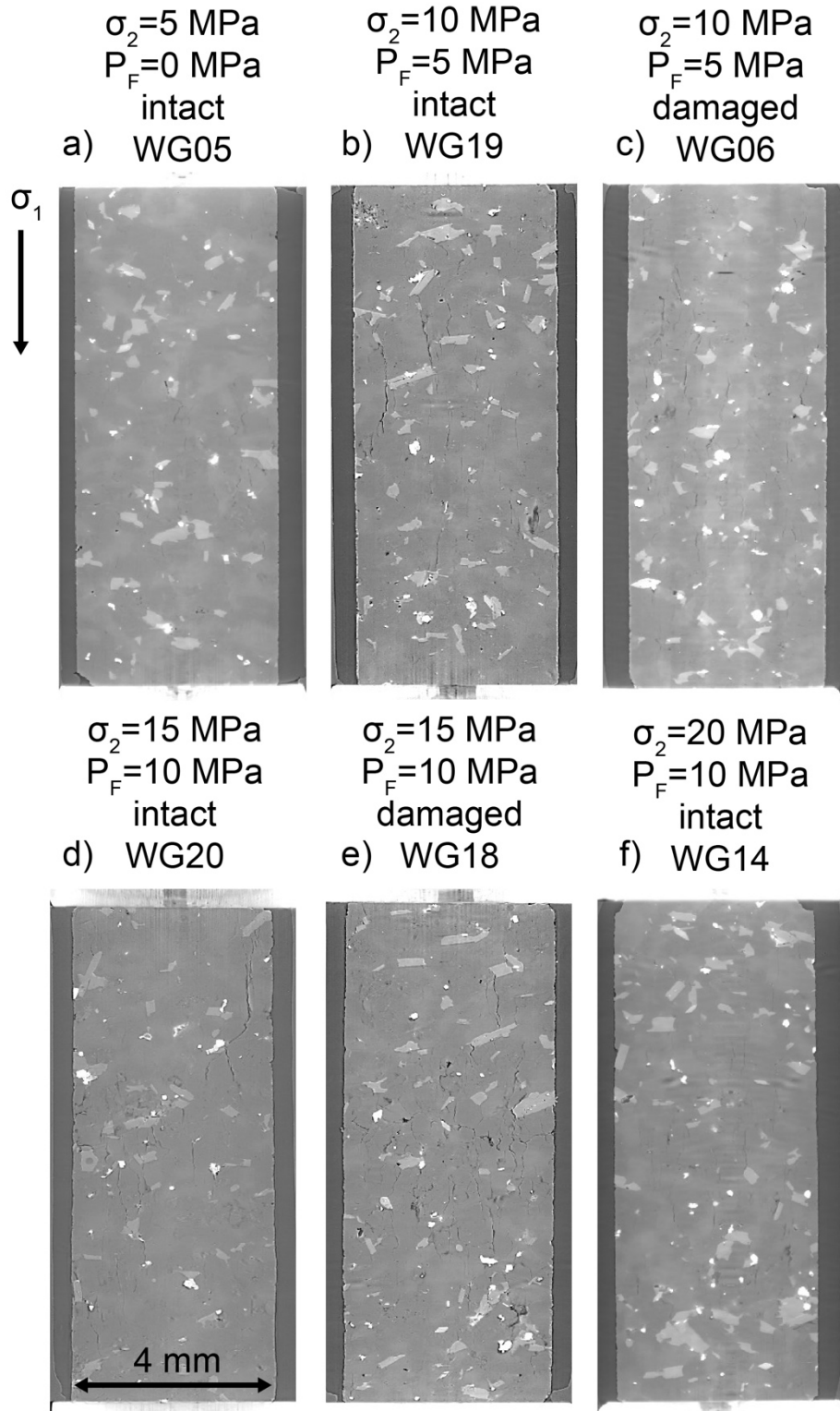120    preexisting highly fractured system.

**Figure 1**. Two-dimensional slices of the tomograms acquired immediately preceding macroscopic failure in the six experiments. Minerals with larger densities, such as oxides and biotite, have larger gray-scale values in the tomograms (lighter gray and white regions), than minerals with lower densities, such as quartz and feldspar (darker gray). The fractures have lower gray-scale values (dark gray and black). The applied confining stress, $\sigma_2$, and fluid pressure, $P_F$, and whether the rock core was damaged or intact are listed above each slice.

128        2.2. Digital volume correlation analysis

129        To calculate the local three-dimensional strain fields, we used the software
130    TomoWarp2 (Tudisco et al., 2017). Digital volume correlation analyses search for similar
131    patterns of voxels in pairs of three-dimensional images and then calculate the displacement
132    vector that maps a pattern in one image to a pattern in another image (e.g., Charalampidou et
133    al., 2011). In TomoWarp2, the node spacing and correlation window size determine the
134    spatial resolution and the size of the volume used to identify similar patterns of voxels,
135    respectively. Calculations with a node spacing of 20 voxels (0.13 mm) and correlation
136    window size of 10 voxels (65 μm) produce an acceptable spatial resolution and reasonable
137    levels of signal to noise (McBeck et al., 2018).

138        To identify the tomograms used in the digital volume correlation analysis, we divide
139    each experiment into 20 equal increments of the macroscopic axial strain, $\varepsilon_{zz}$, and then
140    identify the tomograms with the closest $\varepsilon_{zz}$ to the specified increments (**Figure 2**), following
141    our previous analyses (e.g., McBeck et al., 2018). We then use these pairs of tomograms to
142    perform 19 digital volume correlation calculations for each experiment. The reported strain
143    tensors are thus the local, incremental strains done between each tomogram acquisition, and
144    not the total cumulative strain over the entire experiment. To quantify the localization of the
145    volumetric and deviatoric components of the strain field, we calculate the divergence, $I1$,
146    (volumetric strain, contractive, $I1 < 0$, and dilative, $I1 > 0$) and the second invariant of the
147    deviatoric strain tensor, $J2$, (deviatoric strain, shear) from the incremental displacement
148    fields. In previous analyses, we used the curl of the displacement field to characterize the
149    shear strain, following the technique of the geodetic community (McBeck et al., 2019,
150    2020c). However, recent machine learning analyses suggest that $J2$ may provide more
151    information about the timing of fault reactivation and macroscopic failure in strike-slip fault
152    systems than the curl of the displacement field (McBeck et al 2022a). We also use $J2$ to
153    characterize the shear strain because it determines the maximum distortion criterion, or von
154    Mises yield criterion. Because each tomogram captures regions outside the rock core, such as
155    the jacket and deformation apparatus, we remove the portion of the calculated strain field that
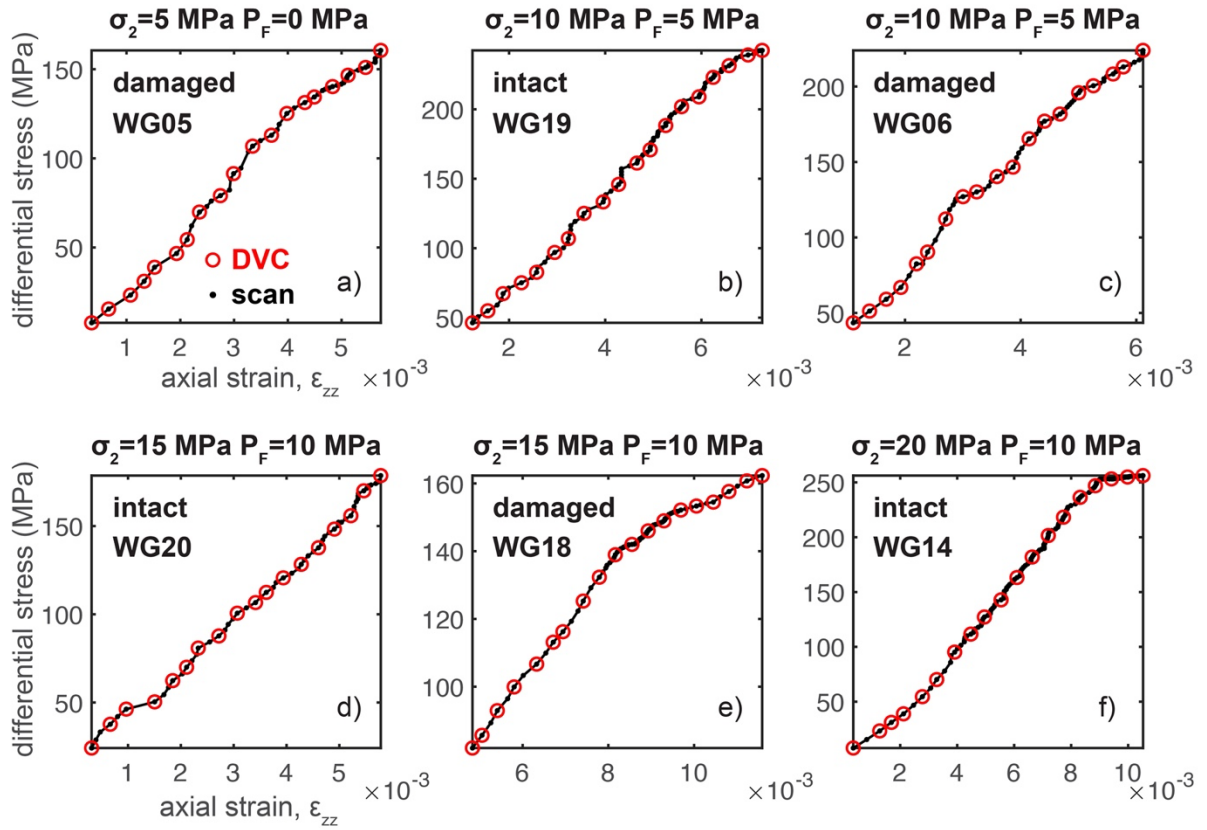156    is outside the rock core.

157

158
159 **Figure 2**. Differential stress and cumulative axial strain, $\varepsilon_{zz}$, when each tomogram or scan
160 was acquired (black symbols) and the conditions of the scans used in the digital volume
161 correlation (DVC) analyses (red symbols) for each experiment. The applied confining stress,
162 $\sigma_2$, fluid pressure, $P_F$, and whether the core was heat-treated (damaged) before the
163 experiment or not (intact) are listed at the top of each plot. The differential stress and $\varepsilon_{zz}$ of
164 the first scans shown here are not zero because we do not show the scans that were acquired
165 during the early phase of each experiment when the axial strain-differential stress curve is
166 highly non-linear and concave upward. This non-linearity is caused in part by the closure of
167 preexisting fractures and pores, and to a larger extent by the settling of the rock core inside
168 the apparatus as it comes in contact with the upper and lower pistons. We only include the
169 scans following this non-linear stage in the digital volume correlation analysis.

170 **3  Results**
171     3.1. Evolution of the spatial localization of the strain components

172         To quantify the spatial localization of the contraction, $|I1 < 0|$, dilation, $I1 > 0$, and
173 shear strain, $J2$, we compare the volume of the polyhedron that surrounds high values of each
174 strain component, $v_h$, to the volume of the polyhedron that surrounds all of the values of the
175 given strain component, $v_t$. For the shear strain, $v_t$ is equal to the volume of the rock core
176 used in the digital volume correlation analysis. For the volumetric strain components, $v_t$ may
177 be smaller than the volume of the rock core because the fraction of the rock core occupied by
178 the dilation or contraction evolves throughout the experiment. Consequently, we first
179 examine the evolution of this volume, $v_t$, divided by the volume of the total rock used in the
180 digital volume correlation analysis for the dilation and contraction throughout each
181 experiment. This comparison also provides insight into the influence of confining stress, $\sigma_2$,
182 on volumetric strain.

183  We report the time in the experiments using the normalized cumulative macroscopic
184  axial strain, $\widetilde{\varepsilon_{zz}}$. We normalize the macroscopic axial strain so that the maximum and
185  minimum values are one and zero. In particular, $\widetilde{\varepsilon_{zz}}$ is calculated from the $\varepsilon_{zz}$ calculated for
186  the given tomogram, the $\varepsilon_{zz}$ of the tomogram acquired immediately preceding macroscopic
187  failure, $\varepsilon_{zz}^{F}$, and the $\varepsilon_{zz}$ of the first tomogram acquired at the onset of the linear phase early in
188  loading, $\varepsilon_{zz}^{0}$, as $\widetilde{\varepsilon_{zz}} = (\varepsilon_{zz} - \varepsilon_{zz}^{0})/(\varepsilon_{zz}^{F} - \varepsilon_{zz}^{0})$.
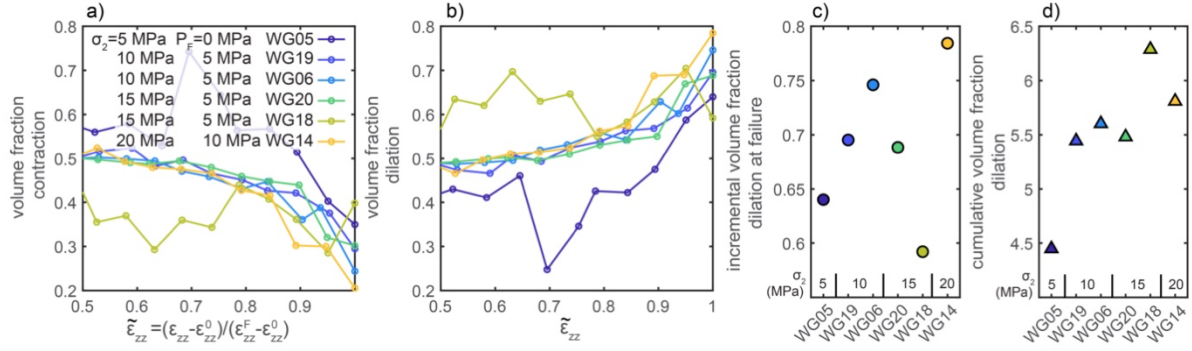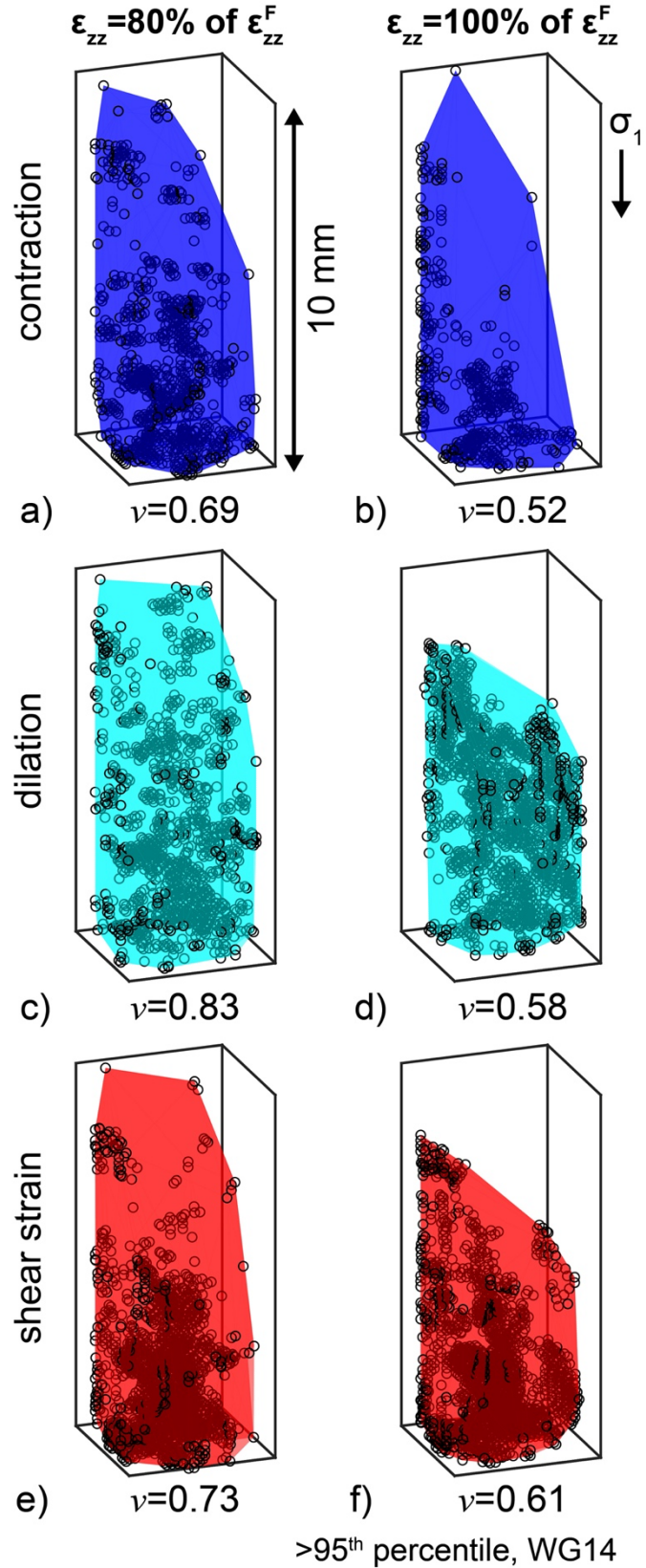
189



190  **Figure 3**. Fraction of the volume of the rock occupied by contraction, $I1 < 0$ (a) and dilation,
191  $I1 > 0$ (b) as a function of the normalized cumulative macroscopic axial strain, $\widetilde{\varepsilon_{zz}}$, of the
192  second tomogram used in each digital volume correlation calculation, and the incremental (c)
193  and sum of the incremental, or cumulative, fraction occupied by dilation (d) at the end of
194  each experiment. The normalized cumulative macroscopic axial strain, $\widetilde{\varepsilon_{zz}}$, is a function of
195  the $\varepsilon_{zz}$ calculated from the given tomogram, the $\varepsilon_{zz}$ of the tomogram acquired immediately
196  preceding macroscopic failure, $\varepsilon_{zz}^{F}$, and the $\varepsilon_{zz}$ of the first tomogram acquired at the onset of
197  the linear phase early in loading, $\varepsilon_{zz}^{0}$, as $\widetilde{\varepsilon_{zz}} = (\varepsilon_{zz} - \varepsilon_{zz}^{0})/(\varepsilon_{zz}^{F} - \varepsilon_{zz}^{0})$. The colors of the
198  symbols indicate different experiments.

199  The volume fraction occupied by contraction generally decreases while the fraction
200  occupied by dilation generally increases after about 0.8 $\widetilde{\varepsilon_{zz}}$ (**Figure 3**). The exception to this
201  trend is experiment WG18. This experiment hosts relatively large volume fractions of
202  dilation, up to 0.7, early in loading, when $\widetilde{\varepsilon_{zz}}$ is about 0.6. This experiment may have unique
203  behavior because as this rock core was loaded into the deformation apparatus, it developed a
204  core-spanning fracture perpendicular to the maximum compressive stress (**Figure S1**).
205  Increasing axial stress during the experiment then closed the fracture.

206  To assess the influence of $\sigma_2$ on the volumetric strains, we compare the incremental
207  volume fraction occupied by dilation immediately preceding failure, derived from the final
208  digital volume correlation calculation, and the sum of the incremental (cumulative) volume
209  fraction from the onset of loading to the end of the experiment. Both the incremental and
210  cumulative strains indicate that larger $\sigma_2$ promotes dilation (**Figure 3c, d**). Experiment
211  WG14, with the largest confining stress ($\sigma_2$=20 MPa) and largest effective stress ($P_e$=10
212  MPa), achieves the largest incremental volume fraction occupied by dilation at the end of the
213  experiment, and immediately preceding failure (**Figure 3c**), and the second largest
214  cumulative volume fraction (**Figure 3d**). Experiment WG05, with the smallest $\sigma_2$ (5 MPa),
215  and smallest $P_e$ (5 MPa), achieves the smallest cumulative and second smallest incremental
216  volume fraction occupied by dilation at the end of the experiment. Experiment WG18, with
217  $\sigma_2$=15 MPa and $P_e$=5 MPa, experiences the smallest incremental volume fraction and largest
218  cumulative volume fraction occupied by dilation. The development of the core-spanning
219  fracture produced a relatively high volume fraction of dilation earlier in loading in this
220  experiment compared to the other experiments. In general, greater $\sigma_2$ and $P_e$ promote dilation.

**Figure 4**. Spatial distribution of the high values (>95th percentile) of the contraction (a, b), dilation (c, d) and shear strain (e, f) at $\varepsilon_{zz}/\varepsilon_{zz}^F$=0.80 (a, c, e), and at $\varepsilon_{zz}/\varepsilon_{zz}^F$=1, immediately preceding macroscopic failure (b, d, f) for experiment WG14. Black circles show the location of the three-dimensional strain field with high values of incremental strain, >95th percentile. Shaded dark blue, light blue and red areas show the convex hull that fits around the high strain values. The numbers below each plot show the fraction of the volume of the convex hull relative to the total volume occupied by all of the values of the strain component, $v$. The $v$ of the contraction, dilation, and shear strain all decrease with increasing differential stress, from 80% to 100% of $\varepsilon_{zz}^F$.

245        As described above, we calculate the volume of the convex hull or polyhedron that
246    surrounds the population of the high strains, $v_h$, for each of the 19 digital volume correlation
247    calculations performed in each experiment in order to quantify the spatial localization of the
248    high strain values. We use this metric, rather than a previous metric we used to quantify the
249    localization of strain (McBeck et al., 2022b), because this metric does not require defining a
250    grid size, and thus the results are independent of this parameter. We report $v_h$ divided by the
251    volume of the polyhedron that surrounds all of the values of the given strain component, $v_t$,
252    as $v = v_h/v_t$. **Figure 4** shows the polyhedrons and resulting $v$ found for the contractive,
253    dilative, and shear strain values greater than the 95th percentile value at two different time
254    steps (and digital volume correlation calculations) in experiment WG14. One of the time
255    steps occurs immediately preceding macroscopic failure, when the $\varepsilon_{zz}$ of the second
256    tomogram used in the digital volume correlation analysis is equal to the $\varepsilon_{zz}$ of the final
257    tomogram acquired in the experiment, $\varepsilon_{zz}^F$, or $\varepsilon_{zz}/\varepsilon_{zz}^F = 1$. The other time step is earlier in
258    the experiment, when $\varepsilon_{zz}/\varepsilon_{zz}^F = 0.8$. These example polyhedrons show that the $v$ of each
259    strain component decreases with increasing differential stress and cumulative axial strain,
260    indicative of localization towards macroscopic failure.

261        **Figure 5** shows $v$ for each strain component and all of the experiments for two of the
262    percentile thresholds used to identify the high strain values, the 50th and 90th percentile. We
263    perform the analyses with six different thresholds (50th, 60th, 70th, 80th, 90th, 95th), and
264    summarize those results in subsequent sections. When the dilation or contraction are greater
265    than the 50th or 90th percentile, all but one or two experiments (WG05 and WG18) host
266    decreases in $v$ after about 0.8 to 0.9 $\widetilde{\varepsilon_{zz}}$. For the shear strain, a smaller number of the
267    experiments host decreases in $v$ toward failure. The decreasing $v$ indicates that the high strain
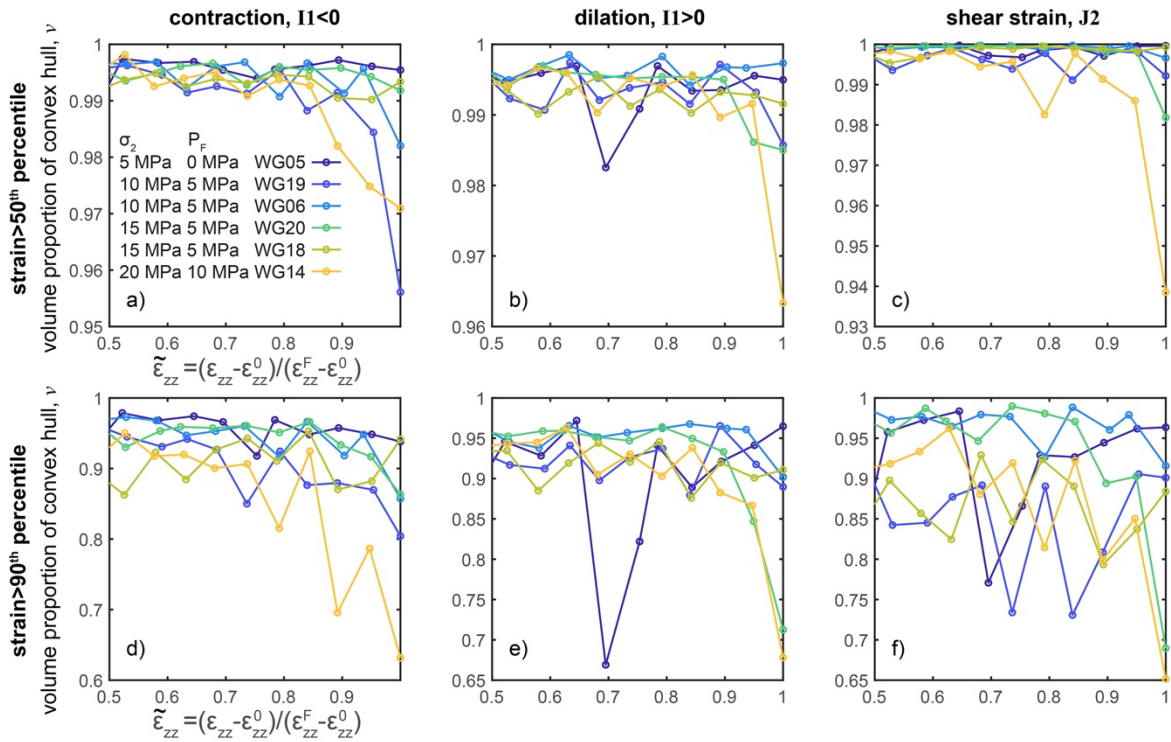268    events localize. We next quantify these decreases in $v$ approaching macroscopic failure.



269    **Figure 5**. Evolution of the volume fraction of the convex hull around the high strain values,
270    $v$, for strains greater than the 50th percentile (a-c) and 90th percentile (d-f), for the absolute

271 value of the contraction, $|I1 < 0|$, (a, d) dilation, $I1 > 0$, (b-e) and shear strain, $J2$ (c, f). The
272 different colors of the curves correspond to the different experiments.

273         To quantify the evolution of $v$, we first examine the cumulative localization
274 approaching macroscopic failure. **Figure 6** shows the absolute value of the sum of the
275 negative values of the change in $v$ from one digital volume correlation calculation to the next,
276 when $\widetilde{\varepsilon_{zz}}>0.5$, $\sum_{\widetilde{\varepsilon_{zz}}=0.5}^{\widetilde{\varepsilon_{zz}}=1} |\Delta v(\Delta v < 0)|$. Negative $\Delta v$ indicates that the volume of the
277 polyhedron that surrounds the high strain events decreases from one digital volume
278 correlation calculation to the next, and thus the high strain events localize from one stress
279 step to the next. We sum the values when $\widetilde{\varepsilon_{zz}}>0.5$, and not from the onset of loading, because
280 we aim to characterize strain localization approaching macroscopic failure. Larger values of
281 the cumulative localization thus indicate greater magnitudes of localization toward
282 macroscopic failure.

283         The cumulative localization increases with the strain threshold (**Figure 6**). The
284 analysis thus detects more localization with larger strain thresholds. This trend is expected
285 because larger strain thresholds produce lower numbers of high strain events. The cumulative
286 localization increases with $\sigma_2$ for the contraction, dilation, and shear strain for all of the
287 thresholds <95th percentile (**Figure 6g-i**). When the threshold is the 95th percentile, the
288 cumulative localization increases with $\sigma_2$ for the contraction and shear strain, but not the
289 dilation (**Figure 6h**). Dividing the experiments into groups with relatively lower and higher
290 $\sigma_2$ helps show that the cumulative localization increases with $\sigma_2$ (**Figure 6d-f**). Using all of
291 the thresholds, the mean of the cumulative localization of the contraction for the experiments
292 with $\sigma_2>10$ MPa is 36% greater than the mean of the experiments with $\sigma_2 \leq 10$ MPa. This
293 difference is 13% and 41% for the dilation and shear strain, respectively. The generally
294 positive slopes of the lines that fit through the cumulative localization and $\sigma_2$ for each strain
295 component and each threshold also indicate that larger $\sigma_2$ produces greater cumulative
296 localization.

297         The results reveal differences in the cumulative localization of the nominally intact
298 rocks and heat-treated, damaged rocks (**Figure 6d-f**). The intact rocks tend to experience
299 more cumulative localization than the damaged rocks. In particular, the mean of the
300 cumulative localization of the intact rocks is 38%, 25%, and 50% greater than the mean of the
301 damaged rocks for the contraction, dilation, and shear strain, respectively.
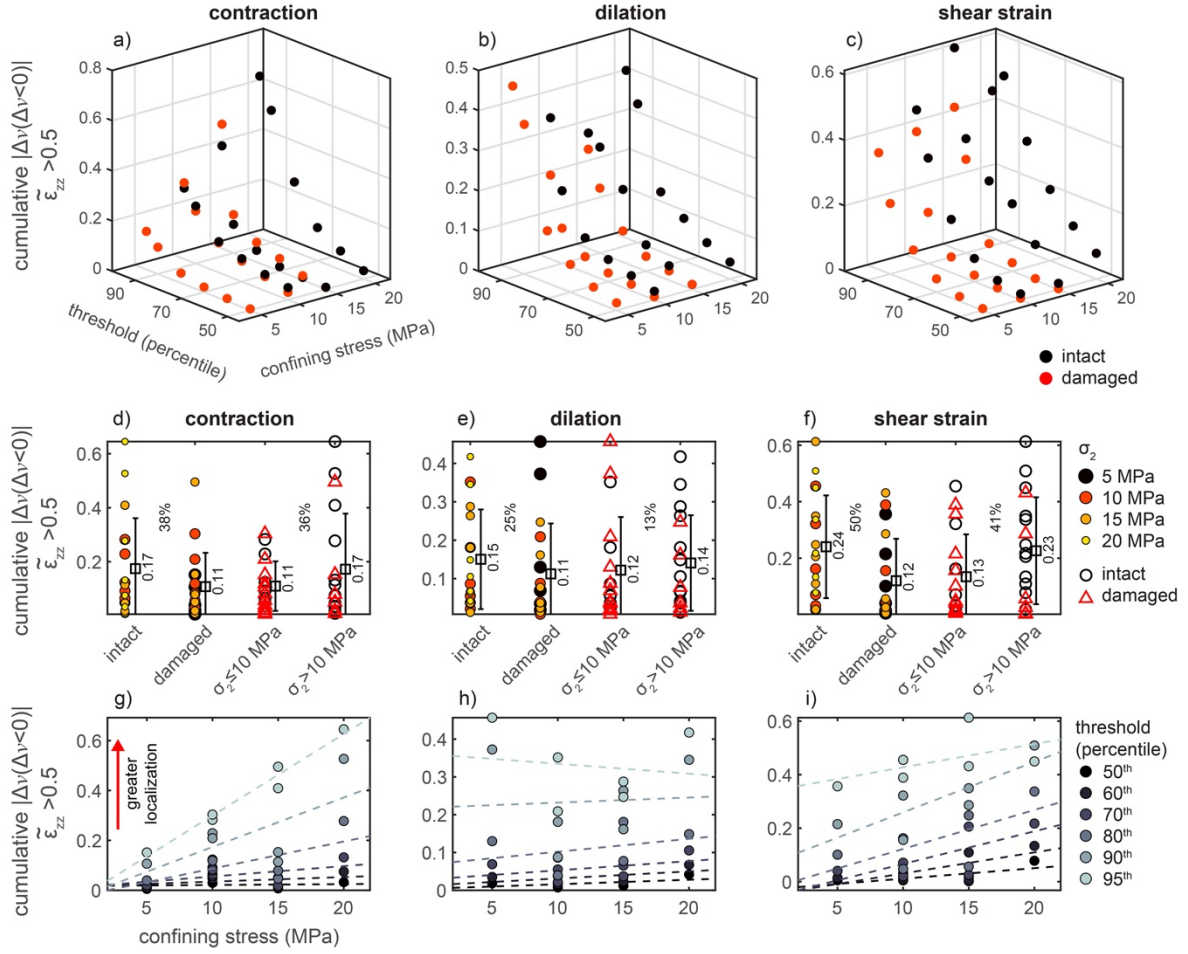
302
303 **Figure 6**. The cumulative localization hosted by each strain component approaching failure,
304 calculated as the sum of the absolute value of the negative change in $v$ when $\widetilde{\varepsilon_{zz}}>0.5$,
305 $\sum_{\widetilde{\varepsilon_{zz}}=0.5}^{\widetilde{\varepsilon_{zz}}=1}|\Delta v(\Delta v<0)|$. Negative $\Delta v$ indicates that the volume of the polyhedron that
306 surrounds the high strain events decreases from one digital volume correlation calculation to
307 the next, and thus the high strain events localize from one stress step to the next. The top row
308 (a-c) shows three-dimensional plots of the cumulative localization as a function of the applied
309 confining stress, $\sigma_2$, and the thresholds used to identify the high strains for the contraction
310 (a), dilation (b), and shear strain (c). The black and red symbols indicate if the sample was
311 intact (black) or damaged (red). The second row (d-f) shows the cumulative localization
312 grouped by the intact and damaged rocks, and experiments with lower $\sigma_2$ ($\leq$10 MPa) and
313 higher $\sigma_2$ (>10 MPa). The color and size of the symbols indicate the $\sigma_2$ for the grouping of
314 the intact and damaged rocks. The black circles and red triangles indicate if the sample was
315 intact (black) or damaged (red) for the grouping of the lower and higher $\sigma_2$. The square
316 symbols and error bars show the mean $\pm$ one standard deviation of each group of data points.
317 The number next to each error bar lists the mean. The percentages between each pair of
318 groups shows the percentage difference between the magnitude of the larger mean, $\mu_{max}$, and
319 smaller mean, $\mu_{min}$, as $(\mu_{max}-\mu_{min})/\mu_{max}$. The third row (g-i) shows the cumulative
320 localization as a function of $\sigma_2$. The color of the symbols indicates the threshold used to
321 identify the high strain values. The dashed lines show the fit of the linear function through the
322 data derived from each threshold. The intact rocks localize by larger amounts than the
323 damaged rocks. Experiments with larger confining stress generally host more localization
324 than experiments with lower confining stress.

325       We also examine alternative methods of quantifying the evolution of $v$ approaching
326  macroscopic failure, in addition to the cumulative localization (**Figure 6**). **Figure 7** shows
327  the localization preceding macroscopic failure measured using the difference in $v$ from the
328  final tomogram acquired immediately preceding failure, when $\widetilde{\varepsilon_{zz}}$ is one, and when $\widetilde{\varepsilon_{zz}}$ is 0.8,
329  $\Delta v$. Negative $\Delta v$ indicates that the high strain events localize towards macroscopic failure.
330  **Figure S2** and **Figure S3** show the $\Delta v$ calculated using $\widetilde{\varepsilon_{zz}}$ of 0.5 and using $\widetilde{\varepsilon_{zz}}$ of 0.9, which
331  produce similar results to those reported for when $\widetilde{\varepsilon_{zz}}$ is 0.8.

332       Using all of the tested combinations of strain components, experiments, high strain
333  thresholds, and selected $\widetilde{\varepsilon_{zz}}$, $\Delta v$ is negative in 75% of the tested combinations. This high rate
334  indicates that the vast majority of strain components localize toward failure. However, this
335  rate varies among the different strain components. For the dilation and contraction, $\Delta v$ is
336  negative in 80% of the tested combinations. For the shear strain, in contrast, $\Delta v$ is negative in
337  only 67% of the tested combinations. Consequently, the volumetric strain components are
338  more likely to experience localization approaching macroscopic failure than the shear strain.

339       The trends observed in this localization metric (**Figure 7**, **Figure S2**, **Figure S3**) are
340  similar to those observed for the cumulative localization (**Figure 6**). The amount of
341  localization increases with the high strain threshold and $\sigma_2$, producing increasingly negative
342  $\Delta v$ (**Figure 7g-i**). Consequently, the experiments with higher $\sigma_2$ localize more than the
343  experiments with lower $\sigma_2$. In addition, the intact rocks localize more than the damaged
344  rocks. The trends observed here also occur when we calculate $\Delta v$ using $\widetilde{\varepsilon_{zz}}$=0.5, and $\widetilde{\varepsilon_{zz}}$=0.9
345  (**Figure S2**, **Figure S3**), and for the $v$ observed in the final digital volume correlation
346  calculation, which captures the strain field immediately preceding macroscopic failure
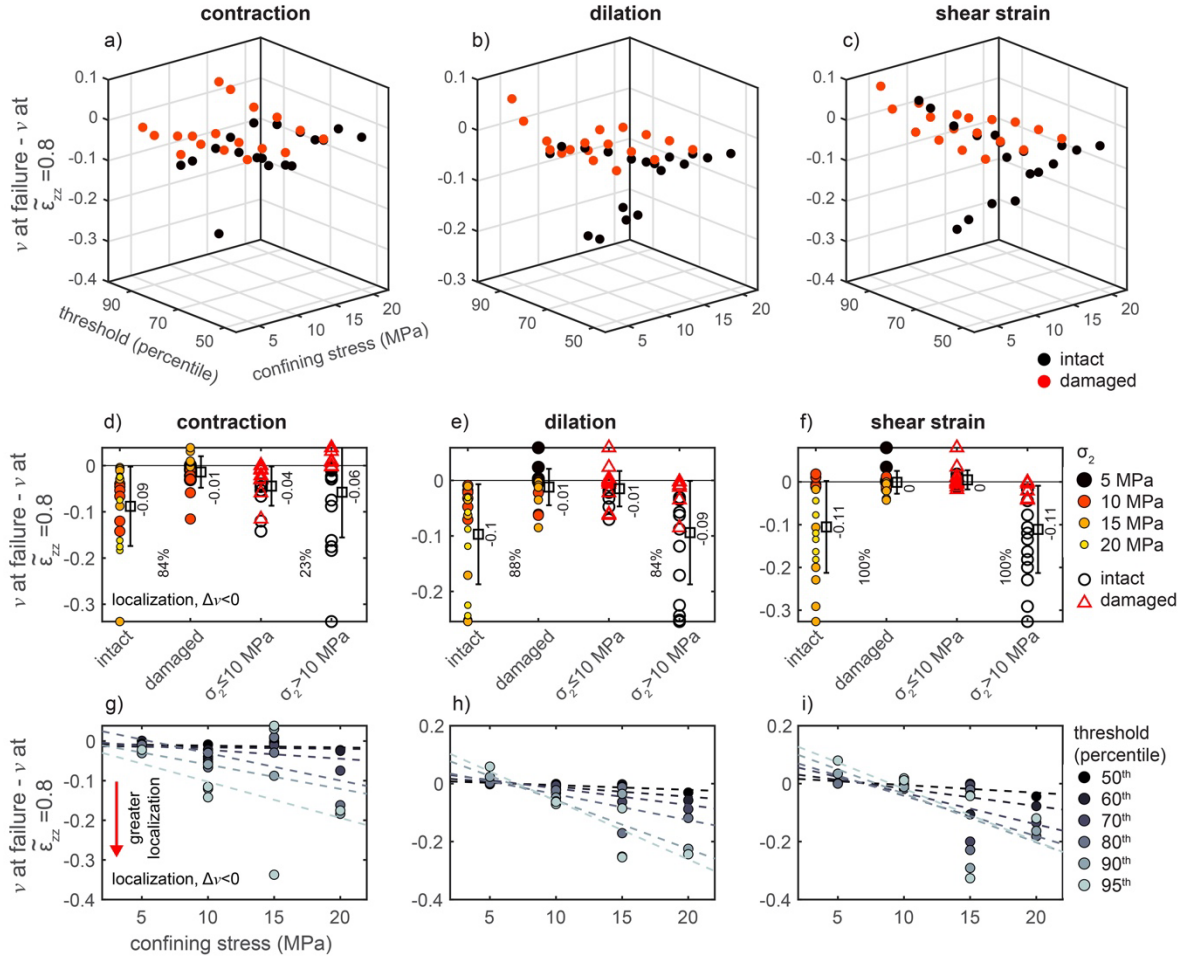347  (**Figure S4**).

348
349 **Figure 7**. Localization immediately preceding failure measured as the difference in $v$ from
350 the final tomogram acquired immediately preceding failure, when $\widetilde{\varepsilon_{zz}}$ is one, and when $\widetilde{\varepsilon_{zz}}$ is
351 0.8, $\Delta v$. Negative $\Delta v$ indicates that the high strain events localize towards macroscopic
352 failure. The format of the figure is the same as **Figure 6**. The intact rocks experience larger
353 amounts of localization preceding macroscopic failure, more negative $\Delta v$, than the damaged
354 rocks. The experiments with larger confining stress host more localization than experiments
355 with lower confining stress.

356 To compare the influence of $\sigma_2$ on localization, we now report the slope of the line
357 that fits $\sigma_2$ and 1) $\Delta v$ from $\widetilde{\varepsilon_{zz}}$=0.5, 0.8 or 0.9 to macroscopic failure, 2) the cumulative
358 localization, and 3) $v$ at the end of each experiment (**Figure 8**). These slopes approximate the
359 influence of $\sigma_2$ on localization near failure for each strain component. **Figure 6**, **Figure 7**,
360 and **Figures S2-S4** show these lines. **Figure S5** shows the slopes derived from all the strain
361 thresholds, and **Figure 8** shows the slopes derived using a threshold of the 90th percentile.
362 Higher percentile thresholds produce larger slopes (**Figure S5**), and so we focus on one
363 percentile here in order to highlight the trends observed for the other percentiles.

364 For each of the localization metrics except the cumulative localization, the dilation
365 and shear strain produce larger negative slopes than the contraction (**Figure 8**). This result
366 indicates that $\sigma_2$ has a stronger influence on the amount of localization near failure for the
367 dilation and shear strain than the contraction. For the cumulative localization, the slopes of
368 the shear strain and contraction are more negative than the slope of the dilation, indicating
369 that $\sigma_2$ has a weaker influence on the amount of cumulative localization approaching failure

370    for the dilation than the shear strain or contraction. The relative magnitudes of the slopes of
371    the cumulative localization may differ from the slopes of the other metrics because the
372    cumulative localization of the experiment WG05, with the lowest $\sigma_2$, is similar to the
373    cumulative localization of the experiments with higher $\sigma_2$. The large and sudden decrease in
374    $v$ for the dilation at $\widetilde{\varepsilon_{zz}}$ of 0.7 produces large cumulative localization for experiment WG05
375    relative to the other experiments with lower $\sigma_2$ (**Figure 5**). This temporary decrease in $v$,
376    however, does not produce similarly anomalous values of $\Delta v$ calculated using $\widetilde{\varepsilon_{zz}}$ of 0.5, 0.8
377    and 0.9, or the $v$ at macroscopic failure. Consequently, the other localization metrics are not
378    influenced by this temporary decrease, and in general, $\sigma_2$ has a larger influence on the
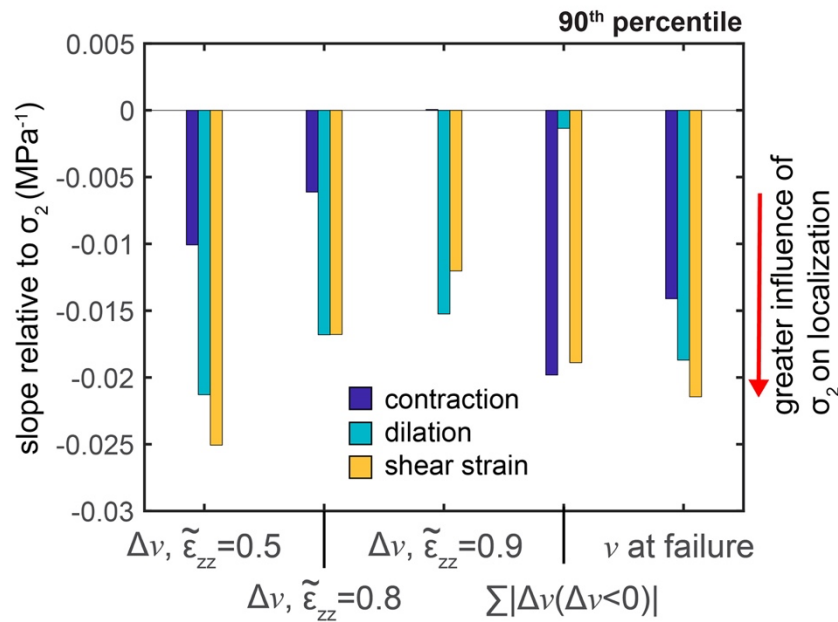379    dilation and shear strain than the contraction.



380

381    **Figure 8**. Slopes of the linear fit of different localization metrics for strains >90th percentile
382    and $\sigma_2$ of the experiments for each strain component: contraction (dark blue), dilation (light
383    blue), and shear strain (yellow). The horizontal axis indicates the localization metrics: 1-3)
384    $\Delta v$ using $\widetilde{\varepsilon_{zz}}$=0.5, $\widetilde{\varepsilon_{zz}}$=0.8, and $\widetilde{\varepsilon_{zz}}$=0.9, 4) the cumulative localization, and 5) $v$ at failure.
385    The slopes derived from the cumulative localization were multiplied by negative one so that
386    larger negative values indicate a stronger influence of $\sigma_2$ on localization for all the metrics.
387    The lines that produce each slope are shown in **Figure 6**, **Figure 7**, **Figure S2**, **Figure S3**,
388    and **Figure S4**. In all but one of the localization metrics, the $\sigma_2$ has a larger influence on the
389    dilation and shear strain than the contraction.

390    3.2. Phases of delocalization and localization

391         The previous section focuses on the change in localization preceding macroscopic
392    failure. Here, we compare the proportion of the experiment time, in terms of $\widetilde{\varepsilon_{zz}}$, that each
393    strain component is localizing, and the timing of when the maximum localization occurs
394    relative to macroscopic failure. In an ideal system that lacks significant heterogeneities, one
395    may expect that the high strain values would continually localize with increasing axial strain
396    or differential stress (Lyakhovsky et al., 2011). Consequently, the proportion of $\widetilde{\varepsilon_{zz}}$ in which
397    the $\Delta v$ from one digital volume correlation calculation to the next is less than zero should be
398    one. However, for all of the tested strain thresholds, strain components, and experiments, this
399    proportion is always less than one, indicating that the high strains experience temporary

400    episodes of delocalization (**Figure 9**). The intact rocks tend to experience localization for a
401    longer proportion of $\widetilde{\varepsilon_{zz}}$ than the damaged rocks (**Figure 9d-f**). On average, the intact rocks
402    experience localization for 13% (contraction), 23% (dilation), and 16% (shear strain) more
403    $\widetilde{\varepsilon_{zz}}$ than the damaged rocks. Thus, the damaged rocks have longer total phases of
404    delocalization than the intact rocks.

405          For the dilation and shear strain, the experiments with higher $\sigma_2$ tend to host
406    localization for a longer period of $\widetilde{\varepsilon_{zz}}$ than the experiments with lower $\sigma_2$. The experiments
407    with $\sigma_2 > 10$ MPa host localization on average for 24% (dilation) and 25% (shear) more $\widetilde{\varepsilon_{zz}}$
408    than the experiments with $\sigma_2 \leq 10$ MPa (**Figure 9f**). For the contraction, the experiments with
409    $\sigma_2 \leq 10$ MPa host slightly longer periods of $\widetilde{\varepsilon_{zz}}$ with localization (8%) than the experiments
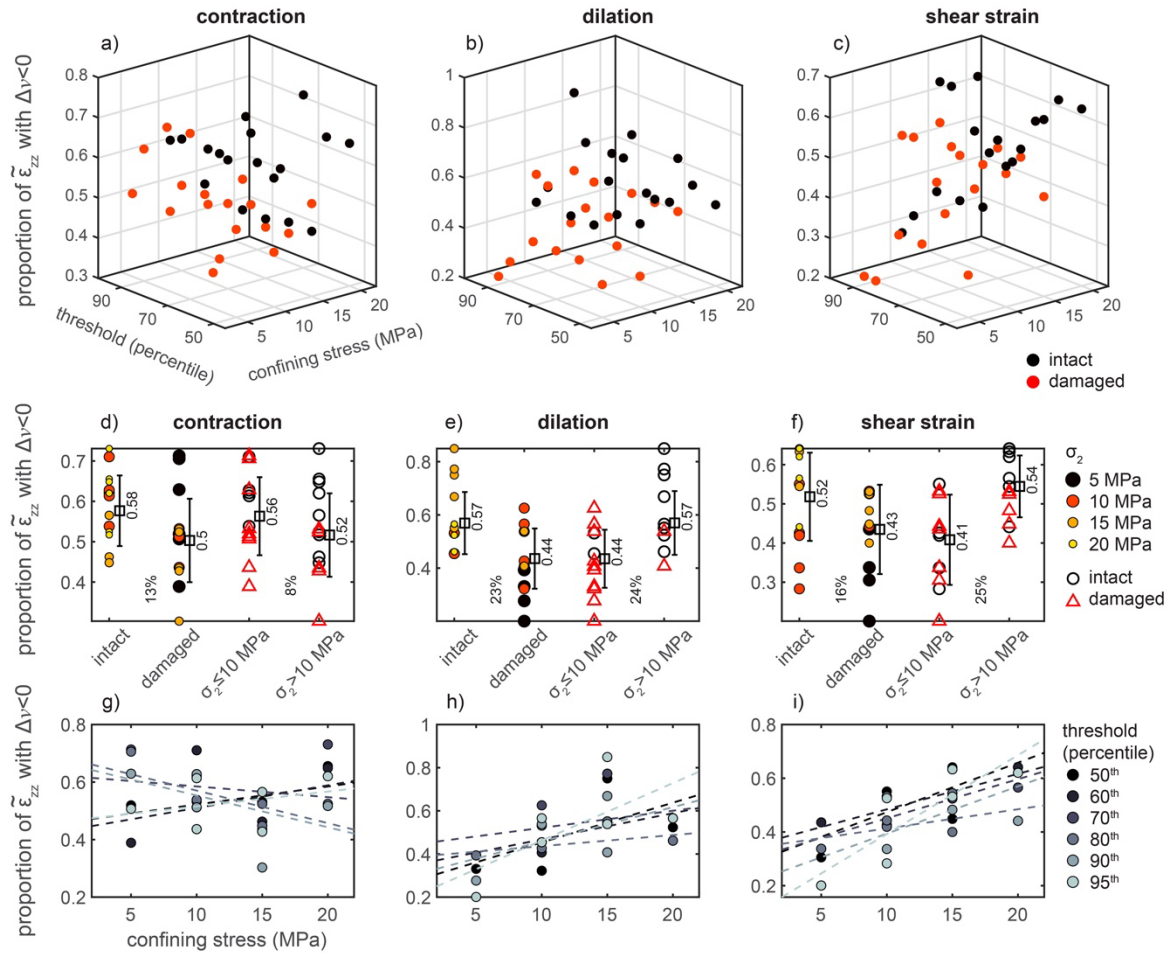410    with $\sigma_2 > 10$ MPa.



411
412    **Figure 9.** Proportion of the experiment time, in terms of $\widetilde{\varepsilon_{zz}}$, in which the strain component
413    produces negative $\Delta v$, and thus localizes. Format is the same as **Figure 6**. The intact rocks
414    experience larger proportions of $\widetilde{\varepsilon_{zz}}$ in which the strain components localize than the
415    damaged rocks. The experiments with larger confining stress generally host more $\widetilde{\varepsilon_{zz}}$ in
416    which the strain components localize.

417          These results indicate that the high strain values do not systematically increase in
418    localization with increasing differential stress or axial strain. Instead, they experience
419    episodes of delocalization, rather than a continuous increase or acceleration of localization
420    toward catastrophic failure. **Figure 10** shows the $\widetilde{\varepsilon_{zz}}$ when each strain component

421 experiences its minimum $v$, and thus maximum localization. The damaged rocks host their
422 maximum localization earlier in loading than the intact rocks (**Figure 10d-f**). The maximum
423 localization occurs on average at $\widetilde{\varepsilon_{zz}}$ of 0.86, 0.72, and 0.79 for the contraction, dilation and
424 shear strain, respectively, of the damaged rocks. In contrast, for the intact rocks, the
425 maximum localization occurs on average at $\widetilde{\varepsilon_{zz}}$ of 1, 0.98, and 0.93 for the contraction,
426 dilation and shear strain, respectively. The differences in $\sigma_2$ produce only small differences in
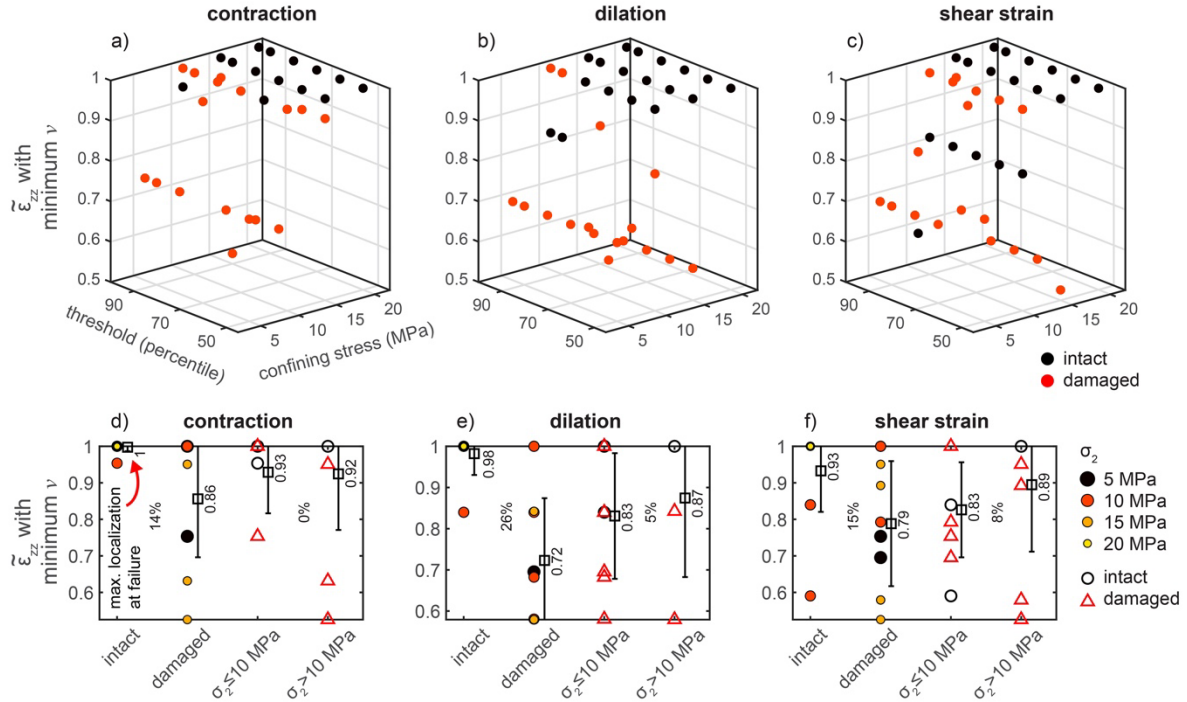427 the timing of the maximum localization.



428
429 **Figure 10**. Timing of the maximum localization, minimum $v$, in terms of $\widetilde{\varepsilon_{zz}}$. Format is the
430 same as **Figure 6** (a-f). The intact rocks tend to host their maximum localization immediately
431 preceding failure, when $\widetilde{\varepsilon_{zz}}$ is one. In contrast, the damaged rocks host their maximum
432 localization earlier in loading.

433 **4  Discussion**
434    4.1. The influence of confining stress on volumetric strain

435        Tracking the volume of the rock occupied by dilation in the experiments on damaged
436 and intact rocks, at confining stresses of 5-20 MPa, and effective stresses of 5 MPa and 10
437 MPa indicates that the volume of rock that experiences dilation generally increases toward
438 failure, particularly after about 0.8 $\widetilde{\varepsilon_{zz}}$ (**Figure 3**). This evolution is consistent with previous
439 digital volume correlation analyses of X-ray tomogram triaxial compression experiments
440 (Renard et al., 2019, McBeck et al., 2019, 2020c). The observed increase of the local,
441 incremental dilation with increasing differential stress is also consistent with previous
442 measurements of the macroscopic, cumulative volumetric strain of Westerly granite during
443 triaxial compression (e.g., Brace et al., 1966, Bieniawski, 1967; Brace, 1978). In triaxial
444 compression experiments on low porosity crystalline rocks, the macroscopic volumetric
445 strain measured from the change in shape of the sample first evolves with the differential
446 stress approximately linearly, with increasingly contractive values, or negative in the adopted
447 sign convention. Then, at the onset of dilatancy, C', which may be about 50-75% of the stress
448 at failure (Brace, 1978), the volumetric strain begins to develop increasingly dilative values,
449 and the macroscopic dilation continually increases until macroscopic failure. The progressive

450  increase of the macroscopic dilation observed following C' in triaxial compression
451  experiments is consistent with the observed acceleration of the volume of rock occupied by
452  dilation observed in the present analysis.

453      Comparing the fraction of the rock core that hosts dilation immediately preceding
454  failure among the experiments indicates that increasing $\sigma_2$ generally promotes greater dilation
455  (**Figure 3**). One may expect that greater $\sigma_2$ would suppress dilation. Indeed, triaxial
456  compression experiments on porous rocks such as Berea sandstone and Adamswiller
457  sandstone show that when $\sigma_2$ increases from 5 MPa to 40 MPa, the cumulative amount of
458  inelastic dilation, which occurs following the onset of dilatancy and until macroscopic failure,
459  decreases (Jamison & Teufel, 1979; Wong et al., 1997). However, for low porosity crystalline
460  rocks, the relationship between $\sigma_2$ and the dilation follows the opposite trend observed in the
461  sandstone (e.g., Brace & Orange, 1968; Crouch, 1970; Paterson & Wong, 2005 p. 70), and
462  the same trend observed in the present experiments. In particular, for Westerly granite and
463  Witwatersrand quartzite, larger $\sigma_2$ increases the inelastic dilation within the range of 3 to 30
464  MPa $\sigma_2$ for the quartzite, and 160 to 500 MPa $\sigma_2$ for the granite (Brace & Orange, 1968;
465  Crouch, 1970). These results highlight a fundamental difference in the accumulation of
466  dilatancy in low porosity crystalline rocks, in which fracture propagation and opening
467  promotes dilatancy, and porous rocks, in which pore collapse and cataclasis may inhibit
468  dilatancy.

469      To compare our results to this previous work, we calculate the amount of inelastic
470  volumetric strain (dilation) that develops between the onset of dilatancy, C' (Brace, 1978),
471  and macroscopic failure using the change in shape of the rock core observed in the X-ray
472  tomograms (**Figure 11a, b**). We then compare these values to the sum of the volume fraction
473  occupied by dilation, and the sum of the mean dilation from the onset of loading until failure
474  calculated from the local incremental strains derived via digital volume correlation (**Figure
475  11c, d**). The identified values of C' are estimates based on the reversal in the slopes of the
476  volumetric strain and differential stress curves. These estimates occur near 75% of the
477  differential stress at failure, consistent with previous observations of the stress at C' (Brace,
478  1978).

479      Examining the macroscopic inelastic volumetric strain indicates that increasing $\sigma_2$
480  generally promotes more inelastic dilation (**Figure 11b**). The two damaged experiments,
481  WG06 and WG18, deviate from the overall trend of increasing inelastic dilation with
482  increasing $\sigma_2$. These experiments produce more inelastic strain than expected from the intact
483  experiments with the corresponding $\sigma_2$. Previous work shows that more preexisting damage
484  generally produces longer macroscopic yielding phases in which more volumetric and axial
485  strain accumulate. In particular, sandstone with some significant porosity accumulates more
486  volumetric and axial strain than granite during triaxial compression (e.g., Feng et al., 2019).
487  Examining the cumulative volume fraction of dilation also shows that the damaged
488  experiments WG06 and WG18 host larger volume fractions of dilation than expected from
489  the corresponding intact experiments (**Figure 11c**). In summary, the cumulative volume
490  fraction (**Figure 11c**), the cumulative mean dilation (**Figure 11d**), and the macroscopic
491  inelastic volumetric strain (**Figure 11b**) all suggest that larger $\sigma_2$ promotes more dilation,
492  consistent with previous measurements of low porosity crystalline rock (e.g., Brace &
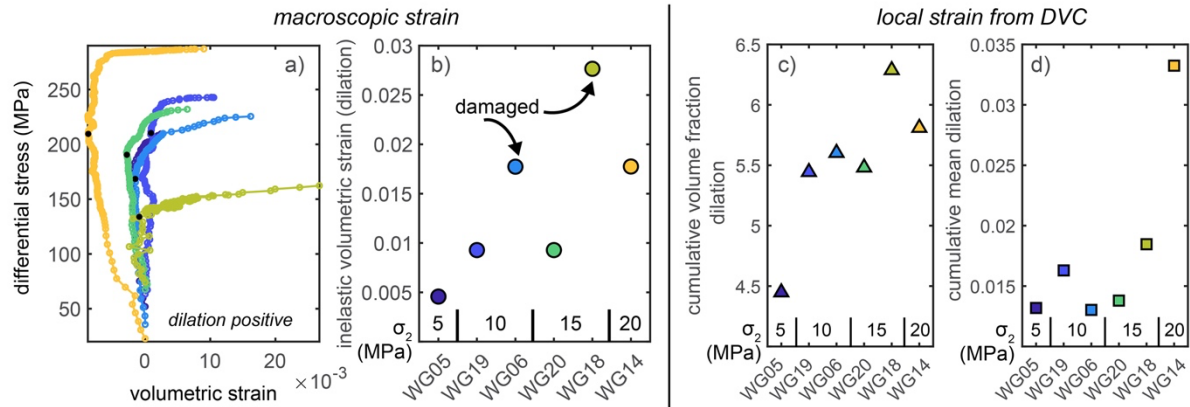493  Orange, 1968; Crouch, 1970).

494
495 **Figure 11**. The influence of $\sigma_2$ on dilatancy. Evolution of the volumetric strain calculated
496 from the shape change of the rock core observed in the X-ray tomograms (a), the amount of
497 inelastic volumetric strain between the onset of dilatancy, C', and macroscopic failure (b),
498 and the cumulative volume fraction of the dilation (c) and cumulative mean dilation (d)
499 calculated from the local strain derived from digital volume correlation. The black dots in (a)
500 shows the location of C'. Increasing $\sigma_2$ produces more dilation.

501     4.2. The influence of confining stress on localization approaching macroscopic failure

502         Tracking the volume of the polyhedron that surrounds the high contraction, dilation
503 and shear strain indicates that the high strain events localize approaching macroscopic failure
504 in all three components for the vast majority of the experiments (**Figure 5**). However, for all
505 the tested parameters, the dilation localizes approaching failure more often (80% of the
506 combinations of parameters produce negative changes in volume) than the shear strain (67%)
507 (e.g., **Figure 6**, **Figure 7**). This result is consistent with a previous analysis of the localization
508 of the volumetric and shear strain in a different set of X-ray tomography experiments on
509 Westerly granite, Fontainebleau sandstone, Mt. Etna basalt, Green River shale, and Anstrude
510 limestone (McBeck et al., 2022b). In this previous analysis and the present analysis, the high
511 magnitudes of the volumetric strains localize to a greater extent than the shear strain. In
512 addition, in the present analysis, the maximum strain localization occurs immediately
513 preceding failure for the dilation, on average at 0.98 $\widetilde{\varepsilon_{zz}}$ for the intact rocks, but occurs earlier
514 in loading for the shear strain, on average at 0.93 $\widetilde{\varepsilon_{zz}}$ for the intact rocks (**Figure 10**). Thus,
515 the dilation hosts more systematic increases in localization towards failure than the shear
516 strain, and the timing of maximum localization occurs almost exactly at macroscopic failure.
517 Consequently, both the previous and present analyses suggest that the high magnitudes of the
518 volumetric strains may provide more reliable information about the timing of catastrophic
519 failure than the shear strain. Indeed, machine learning analyses indicate that the evolution of
520 the dilative strain helps predict the timing of macroscopic failure in X-ray tomography
521 experiments, and that the shear strain provides less useful information about the timing of
522 failure (McBeck et al., 2020a). However, machine learning analyses of three-dimensional
523 discrete element method numerical models of segmented fault networks within shear zones
524 indicate that the shear strain provides more useful information about the timing of fault
525 reactivation and macroscopic failure than the volumetric strain (McBeck et al., 2022a).
526 Consequently, the utility of the volumetric strains for predicting the timing of failure may
527 depend on the tectonic environment, and the existence of system-spanning, macroscopic
528 faults.

529         Comparing the degree of localization near failure among the different experiments
530 indicates that higher $\sigma_2$ promotes greater localization approaching macroscopic failure

531    (**Figure 5**, **Figure 6**, **Figure 7**, **Figures S2-S5**). In the brittle portion of the crust, strike-slip
532    faults tend to develop flower structures: a diffuse network of fractures near the surface that
533    then localizes into a narrower zone at depth (Harding, 1985; Sylvester, 1988; Le Guerroue &
534    Cobbold, 2006, Rockwell & Ben-Zion, 2007) (**Figure 12a**). This structure implies that
535    increasing confining stress promotes localization. In addition, seismic observations indicate
536    that low velocity zones surrounding large crustal faults, such as the San Jacinto fault (Wang
537    et al., 2019), can narrow with depth. Moreover, low magnitude seismicity between large
538    magnitude earthquakes in southern and Baja California increases in localization with
539    increasing depth (Ben-Zion & Zaliapin, 2019). Such fault zones are the result of the
540    accumulation of many cycles of fault growth, including coseismic slip and precursory
541    localization. Here, we show that in one cycle of precursory deformation leading to
542    macroscopic failure, greater confining stress leads to greater localization of the high strain
543    events.

544          Observations of post-mortem fracture networks that form in uniaxial and triaxial
545    compression experiments support the idea that increasing confining stress promotes
546    localization (e.g., Paterson, 1958; Paterson & Wong, 2005 p. 212). Under uniaxial
547    compression and low confining stresses in triaxial compression, rock cores fail by axial
548    splitting, in which arrays of fractures aligned parallel to the maximum compression direction
549    develop (e.g., **Figure 12b**). These fracture networks are often diffusely distributed, with
550    several fractures extending from the top to the bottom of the core (e.g., Akdag et al., 2021;
551    Basu et al. 2013; Hu et al., 2021). Under higher confining stresses, the rock cores fail through
552    the development of one or a few macroscopic shear fractures, perhaps as a pair as conjugate
553    shear fractures (e.g., Paterson, 1958; Lee & Rathnaweera, 2016). Although these fractures
554    may develop from the coalescence of many small fractures, the final fracture geometry
555    identified following the maximum stress consists of a few system-spanning fractures.
556    Consequently, the fracture geometries that develop under uniaxial compression and low
557    confining stress tend to be less localized than the fracture geometries that develop at higher
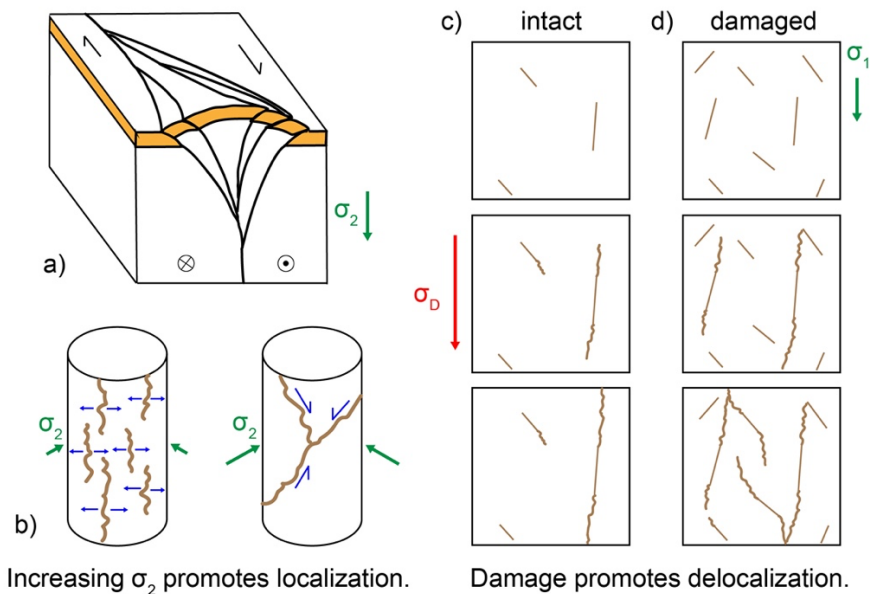558    confining stresses.



559

560    **Figure 12.** Examples of increasing confining stress promoting localization (a-b), and
561    preexisting damage promoting delocalization (c-d). a) Positive flower structures that develop
562    along strike-slip fault networks host a diffuse network of fractures at the surface that localize

563 into a narrower zone with depth. b) The tensile-dominated fracture networks that develop
564 under low confining stress or uniaxial compression tend to be more diffusely spread (left)
565 than the shear-dominated fracture networks that coalesce under higher confining stress
566 (right). c) With lower amounts of preexisting damage, only a few of the longest and most
567 favorably oriented fractures grow under increasing differential stress. d) With more
568 preexisting damage, several of the smaller fractures may grow, rather than the few longest
569 fractures, thereby producing delocalization.

570 A network of fractures dominated by shear may be more localized than a network
571 dominated by tension because the stress concentrations that develop at preexisting fractures
572 and heterogeneities may be more important for the coalescence of shear fractures than the
573 propagation of extensile fractures. Because the tensile strength of rocks is lower than the
574 shear strength (Paterson & Wong, 2005 p. 22), extensile fractures may more easily develop
575 throughout the rock core than shear fractures. Shear fractures may thus depend on the stress
576 concentrations that develop near preexisting fractures in order to propagate and coalesce to a
577 greater extent than the extensile fractures. Consequently, the shear fractures may be more
578 likely to develop near preexisting fractures than the extensile fractures, producing more
579 localized fault networks. Consistent with these theoretical arguments, laboratory
580 observations, and crustal observations of fault structures at depth, the present analysis shows
581 that increasing confining stress promotes greater increases in localization of the high strain
582 events approaching macroscopic failure.

583 4.3. The influence of preexisting damage on localization approaching macroscopic failure

584 The present analysis shows that rocks can experience temporary episodes of
585 delocalization, rather than a continuous increase or acceleration of localization toward
586 catastrophic failure (e.g., **Figure 5**). This result is consistent with previous analyses of
587 fracture development (McBeck et al., 2021a) and strain localization (McBeck et al., 2022b) in
588 X-ray tomography triaxial compression experiments. This previous analysis found that the
589 maximum strain localization generally occurs near 90% of the differential stress at
590 macroscopic failure, rather than at macroscopic failure (McBeck et al., 2022b). In particular,
591 only 46% of the experiments achieve maximum localization at macroscopic failure, or >99%
592 of the failure stress. These results are similar to the damaged rocks in present analysis. For
593 the damaged rocks, the maximum strain localization occurs on average at 94% (contraction),
594 86% (dilation), and 90% (shear strain) of the differential stress at failure. In contrast, for the
595 intact rocks, the maximum strain localization occurs immediately preceding failure, and on
596 average at 99% (contraction and dilation), and 95% (shear strain) of the differential stress at
597 failure (**Figure 10**).

598 The results of the previous analysis (McBeck et al., 2022b) may be more consistent
599 with the results of the damaged Westerly granite than the intact Westerly granite because the
600 majority of the experiments used in the previous analysis were performed on rocks with more
601 preexisting pores and fractures than the intact Westerly granite, such as Fontainebleau
602 sandstone and Mt. Etna basalt. The localization behavior of sandstone and basalt is expected
603 to be more similar to damaged Westerly granite than intact Westerly granite because the
604 presence of preexisting damage can influence fracture development (e.g., Helgeson & Aydin,
605 1991; Tang et al., 2000; d'Alession & Martel, 2004; Gudmundsson et al., 2010; Cartwright-
606 Taylor et al., 2020; Vasseur et al., 2015), and deformation localization (McBeck et al.
607 2021b). For example, analyses of fracture development JGENT in numerical models show that more
608 heterogeneous models produce more precursors than less heterogeneous models (Tang et al.,
609 2000). The precursors in the more heterogeneous models develop in a diffuse distribution

610    early in loading, and then coalesce into a system-spanning fracture that ultimately causes
611    macroscopic failure. In contrast, in less heterogeneous models, only a few precursors develop
612    at random positions throughout the rock, and these positions do not help indicate the final
613    geometry of the system-spanning fracture that causes macroscopic failure. These numerical
614    results are consistent with observations of fracture network development in X-ray
615    tomography triaxial compression experiments on nominally intact and heat-treated (damaged)
616    Ailsa Craig microgranite (Cartwright-Taylor et al., 2020). These experiments show that the
617    heat-treated, and thus more heterogeneous, rock develops more precursory fractures
618    throughout loading toward failure, producing a smooth, continuous evolution, indicative of a
619    second-order transition (Cartwright-Taylor et al., 2020). In contrast, the nominally intact rock
620    hosts few detectable precursors preceding macroscopic failure, producing an abrupt, or first-
621    order, transition. Similarly, numerical models of strike-slip faults embedded in host rock with
622    varying amounts of preexisting weaknesses show that the fracture networks in more
623    homogeneous models continually increase in localization toward macroscopic failure
624    (McBeck et al., 2021b). In contrast, more heterogeneous models experience phases of
625    delocalization superposed on the overall trend of increasing localization. Observations of
626    low-magnitude seismicity preceding several $M>7$ earthquakes in Southern and Baja
627    California reveal similar phases of delocalization (Ben-Zion & Zaliapin, 2020).

628         Consistent with the observed influence of heterogeneities on fracture development
629    and localization, the present analysis shows that the damaged Westerly granite experiences
630    maximum localization earlier in loading than the intact Westerly granite (**Figure 10**).
631    Moreover, the proportion of the macroscopic axial strain in which the intact rocks experience
632    localization is larger than the proportion in which the damaged rocks experience localization
633    (**Figure 9**). In addition, the intact rocks tend to experience more cumulative localization
634    throughout loading (**Figure 6**), greater increases in localization immediately preceding failure
635    (**Figure 7**), and smaller $v$ and thus greater absolute localization at failure (**Figure S4**) than
636    the damaged rocks. Thus, more preexisting damage favors delocalization.

637         The damaged rocks, and more heterogeneous systems in general, may promote
638    episodes of delocalization because the stress concentrations that develop at heterogeneities
639    may allow fracture propagation to require less energy in a network with many smaller
640    fractures than in a more sparsely populated fracture network with several large fractures and
641    only a few smaller fractures (e.g., **Figure 11c**). This effect produces the decreasing strength
642    of rocks at increasing length-scales (e.g., Lockner, 1995; Paterson & Wong, 2005 p. 31).
643    Because larger rock volumes are more likely to contain longer fractures than smaller rock
644    volumes, these longer fractures develop stress concentrations that trigger fracture
645    propagation, and ultimately produce macroscopic failure at a lower level of stress than
646    smaller rock volumes. Consequently, the existence of a diffuse network of heterogeneities
647    enables propagation from many smaller fractures that may delocalize the overall deformation
648    away from the few largest fractures. A diffuse fracture network would also provide a greater
649    opportunity for stress shadows to inhibit growth between fractures (e.g., Nur, 1982) than a
650    more clustered network, and thereby promote delocalization.

651    **5  Conclusions**

652         To assess the influence of confining stress and preexisting damage on strain
653    localization, we perform a series of X-ray tomography triaxial compression experiments on
654    Westerly granite, and then use digital volume correlation to estimate the local three-
655    dimensional strain tensors throughout loading until macroscopic failure. We examine the
656    evolving volume of the polyhedron that surrounds the highest values of three strain

657    components: the contraction, dilation, and shear strain. We find that experiments with higher
658    confining stress (>10 MPa) host larger amounts of dilation than experiments with lower
659    confining stress, consistent with previous laboratory analyses on low porosity crystalline rock
660    (e.g., Brace & Orange, 1968; Crouch, 1970). Higher confining stress is also associated with
661    larger increases in localization of the high strain events approaching macroscopic failure.
662    This positive correlation between confining stress and localization is consistent with the
663    localized geometry of the shear-dominated fractures that develop at higher confining stresses
664    compared to the more diffuse arrangement of the extensile-dominated fractures that develop
665    in uniaxial compression (e.g., Paterson, 1958), and with crustal observations of strike-slip
666    fault networks that narrow with depth (e.g., Sylvester, 1988; Rockwell & Ben-Zion, 2007).
667    Tracking the volume of the high strains shows that the strain events do not always
668    systematically increase in localization towards failure, but instead experience phases of
669    delocalization. This result is consistent with previous X-ray tomography triaxial compression
670    experiments (McBeck et al., 2021a; McBeck et al., 2022b), and with observations of low
671    magnitude seismicity in Southern and Baja California (Ben-Zion & Zaliapin, 2020). The
672    amount of preexisting damage controls the extent of the phases of delocalization, and when
673    the rock experiences the greatest localization of the high strain events. The damaged rocks
674    experience longer proportions of the experiment time, in terms of the macroscopic axial
675    strain, in which the strains are delocalizing than the intact rocks. The heat-treated, and thus
676    damaged, Westerly granite experiments host the greatest localization of the high strain events
677    on average near 90% of the differential stress at failure, consistent with strain localization in
678    rocks with some preexisting porosity and heterogeneities, such as Mt. Etna basalt and
679    Fontainebleau sandstone (McBeck et al., 2022b). In contrast, the intact Westerly granite
680    experiments host the greatest localization of the high strain events on average near 99% of
681    the differential stress at failure. In addition, the high strain events localize by larger
682    magnitudes preceding failure in the intact rocks than the damaged rocks. Consequently, more
683    preexisting damage favors delocalization. More preexisting damage may allow more
684    delocalization because the stress concentrations that develop at preexisting heterogeneities
685    periodically enable smaller fractures to propagate, and form stress shadows that inhibit
686    growth. The results show that the dilation hosts more systematic increases in localization
687    towards failure than the shear strain, consistent with a previous digital volume correlation
688    analysis (McBeck et al., 2022b), and that the timing of maximum localization occurs almost
689    exactly at macroscopic failure, consistent with a machine learning analysis that found that the
690    dilative strain helps predict the timing of catastrophic failure better than the shear strain
691    (McBeck et al., 2020a). Consequently, the dilative strain may provide more reliable
692    information about the timing of catastrophic failure than the shear strain.

### Open Research

701    The experimental data (time series of X-ray tomograms) are available on Norstore with DOI
702    10.11582/2023.00007
703    (https://archive.norstore.no/pages/public/datasetDetail.jsf?id=10.11582/2023.00007).

## References

704  Akdag, S., Karakus, M., Nguyen, G. D., Taheri, A., & Bruning, T. (2021). Evaluation of the
705  propensity of strain burst in brittle granite based on post-peak energy analysis. Underground
706  Space, 6(1), 1-11.

708  Basu, A., Mishra, D. A., & Roychowdhury, K. (2013). Rock failure modes under uniaxial
709  compression, Brazilian, and point load tests. Bulletin of Engineering Geology and the
710  Environment, 72, 457-475.

711  Ben-Zion, Y. and I. Zaliapin, (2019). Spatial variations of rock damage production by
712  earthquakes in southern California, Earth and Planetary Science Letters, 512, 184–193.

713  Ben-Zion, Y., & Zaliapin, I. (2020). Localization and coalescence of seismicity before large
714  earthquakes. Geophysical Journal International, 223(1), 561-583.

715  Benson, P. M., Thompson, B. D., Meredith, P. G., Vinciguerra, S., & Young, R. P. (2007).
716  Imaging slow failure in triaxially deformed Etna basalt using 3D acoustic-emission location
717  and X-ray computed tomography. Geophysical Research Letters, 34(3), L03303.

718  Bieniawski, Z. T. (1967). Mechanism of brittle fracture of rock: Part I. Theory of the fracture
719  process. Part II. Experimental studies; Part III. Fracture in tension and under long-term
720  loading. International Journal of Rock Mechanics and Mining Sciences & Geomechanics
721  Abstracts, 4(4), 395-406.

722  Brace, W. F. (1978). Volume changes during fracture and frictional sliding: A review. Pure
723  and Applied Geophysics, 116, 603-614.

724  Brace, W. F., & Orange, A. S. (1968). Electrical resistivity changes in saturated rocks during
725  fracture and frictional sliding. Journal of Geophysical Research, 73(4), 1433-1445.

726  Brace, W. F., Paulding Jr, B. W., & Scholz, C. H. (1966). Dilatancy in the fracture of
727  crystalline rocks. Journal of Geophysical Research, 71(16), 3939-3953.

728  Buades, A., Coll, B., & Morel, J. M. (2005). A non-local algorithm for image denoising. In
729  2005 IEEE Computer Society Conference on Computer Vision and Pattern Recognition
730  (CVPR'05), 2, 60-65.

731  Cartwright-Taylor, A., Main, I. G., Butler, I. B., Fusseis, F., Flynn, M., & King, A. (2020).
732  Catastrophic failure: how and when? Insights from 4-D in situ x-ray microtomography.
733  Journal of Geophysical Research: Solid Earth, 125(8), e2020JB019642.

734  Charalampidou, E. M., Hall, S. A., Stanchits, S., Lewis, H., & Viggiani, G. (2011).
735  Characterization of shear and compaction bands in a porous sandstone deformed under
736  triaxial compression. Tectonophysics, 503(1-2), 8-17.

737  Crouch, S. L. (1970). Experimental determination of volumetric strains in failed rock. In
738  International Journal of Rock Mechanics and Mining Sciences & Geomechanics Abstracts,
739  7(6), 589-603.

740  d'Alessio, M. A., & Martel, S. J. (2004). Fault terminations and barriers to fault growth.
741  Journal of Structural Geology, 26(10), 1885-1896.

742  Feng, X. T., Kong, R., Zhang, X., & Yang, C. (2019). Experimental study of failure
743  differences in hard rock under true triaxial compression. Rock Mechanics and Rock
744  Engineering, 52, 2109-2122.

745  Fredrich, J. T., & Wong, T. F. (1986). Micromechanics of thermally induced cracking in
746  three crustal rocks. Journal of Geophysical Research: Solid Earth, 91(B12), 12743-12764.

747  Griffiths, L., Heap, M. J., Baud, P., & Schmittbuhl, J. (2017). Quantification of microcrack
748  characteristics and implications for stiffness and strength of granite. International Journal of
749  Rock Mechanics and Mining Sciences, 100, 138-150.

750  Gudmundsson, A., Simmenes, T. H., Larsen, B., & Philipp, S. L. (2010). Effects of internal
751  structure and local stresses on fracture propagation, deflection, and arrest in fault zones.
752  Journal of Structural Geology, 32(11), 1643-1655.

753  Gueydan, F., Précigout, J., & Montesi, L. G. (2014). Strain weakening enables continental
754  plate tectonics. Tectonophysics, 631, 189-196.

755  Harding, T. P. (1985). Seismic characteristics and identification of negative flower structures,
756  positive flower structures, and positive structural inversion. AAPG bulletin, 69(4), 582-600.

757  Helgeson, D. E., & Aydin, A. (1991). Characteristics of joint propagation across layer
758  interfaces in sedimentary rocks. Journal of Structural Geology, 13(8), 897-911.

759  Hu, J., Zeng, P., Yang, D., Wen, G., Xu, X., Ma, S., Zhao, F., & Xiang, R. (2021).
760  Experimental investigation on uniaxial compression mechanical behavior and damage
761  evolution of pre-damaged granite after cyclic loading. Energies, 14(19), 6179.

762  Jamison, W. R., & Teufel, L. W. (1979). Pore volume changes associated with failure and
763  frictional sliding of a porous sandstone. 20th US Symposium on Rock Mechanics (USRMS).
764  OnePetro.

765  Le Guerroué, E., & Cobbold, P. R. (2006). Influence of erosion and sedimentation on strike-
766  slip fault systems: insights from analogue models. Journal of Structural Geology, 28(3), 421-
767  430.

768  Lee, B., & Rathnaweera, T. D. (2016). Stress threshold identification of progressive
769  fracturing in Bukit Timah granite under uniaxial and triaxial stress conditions. Geomechanics
770  and Geophysics for Geo-Energy and Geo-Resources, 2, 301-330.

771  Lockner, D. A. (1995). Rock failure: Rock Physics and Phase Relations. A Handbook of
772  Physical Constants. Am. Geophys. Union Reference Shelf. Am. Geophys. Union, 127-141.

773  Lockner, D., Byerlee, J. D., Kuksenko, V., Ponomarev, A., & Sidorin, A. (1991). Quasi-static
774  fault growth and shear fracture energy in granite. Nature, 350(6313), 39-42.

775  Lyakhovsky, V., Hamiel, Y., & Ben-Zion, Y. (2011). A non-local visco-elastic damage
776  model and dynamic fracturing. Journal of the Mechanics and Physics of Solids, 59(9), 1752-
777  1776.

778  McBeck, J., Aiken, J. M., Ben-Zion, Y., & Renard, F. (2020a). Predicting the proximity to
779  macroscopic failure using local strain populations from dynamic in situ X-ray tomography
780  triaxial compression experiments on rocks. Earth and Planetary Science Letters, 543, 116344.

781  McBeck, J. A., Aiken, J. M., Mathiesen, J., Ben-Zion, Y., & Renard, F. (2020b). Deformation
782  precursors to catastrophic failure in rocks. Geophysical Research Letters, 47(24),
783  e2020GL090255.

784  McBeck, J., Ben-Zion, Y., & Renard, F. (2020c). The mixology of precursory strain
785  partitioning approaching brittle failure in rocks. Geophysical Journal International, 221(3),
786  1856-1872.

787  McBeck, J., Ben-Zion, Y., & Renard, F. (2021a). Fracture network localization preceding
788  catastrophic failure in triaxial compression experiments on rocks. Frontiers in Earth Science,
789  9, 778811.

790 McBeck, J., Ben-Zion, Y., & Renard, F. (2022a). Predicting fault reactivation and
791 macroscopic failure in discrete element method simulations of restraining and releasing step
792 overs. Earth and Planetary Science Letters, 593, 117667.

793 McBeck, J., Ben-Zion, Y., & Renard, F. (2022b). Volumetric and shear strain localization
794 throughout triaxial compression experiments on rocks. Tectonophysics, 822, 229181.

795 McBeck, J., Ben-Zion, Y., Zhou, X., & Renard, F. (2021b). The influence of preexisting host
796 rock damage on fault network localization. Journal of Structural Geology, 153, 104471.

797 McBeck, J. A., Cordonnier, B., Vinciguerra, S., & Renard, F. (2019). Volumetric and shear
798 strain localization in Mt. Etna basalt. Geophysical Research Letters, 46(5), 2425-2433.

799 McBeck, J., Kobchenko, M., Hall, S. A., Tudisco, E., Cordonnier, B., Meakin, P., & Renard,
800 F. (2018). Investigating the onset of strain localization within anisotropic shale using digital
801 volume correlation of time-resolved X-ray microtomography images. Journal of Geophysical
802 Research: Solid Earth, 123(9), 7509-7528.

803 Mulyukova, E., & Bercovici, D. (2019). The generation of plate tectonics from grains to
804 global scales: A brief review. Tectonics, 38(12), 4058-4076.

805 Nur, A. (1982). The origin of tensile fracture lineaments. Journal of Structural Geology, 4(1),
806 31-40.

807 Paterson, M. S. (1958). Experimental deformation and faulting in Wombeyan marble.
808 Geological Society of America Bulletin, 69(4), 465-476.

809 Paterson, M. S., & Wong, T. F. (2005). Experimental rock deformation: the brittle field, 348.
810 Berlin: Springer.

811 Renard, F., Cordonnier, B., Dysthe, D. K., Boller, E., Tafforeau, P., & Rack, A. (2016). A
812 deformation rig for synchrotron microtomography studies of geomaterials under conditions
813 down to 10 km depth in the Earth. Journal of Synchrotron Radiation, 23(4), 1030-1034.

814 Renard, F., McBeck, J., Kandula, N., Cordonnier, B., Meakin, P., & Ben-Zion, Y. (2019).
815 Volumetric and shear processes in crystalline rock approaching faulting. Proceedings of the
816 National Academy of Sciences, 116(33), 16234-16239.

817 Rockwell, T. K., & Ben-Zion, Y. (2007). High localization of primary slip zones in large
818 earthquakes from paleoseismic trenches: Observations and implications for earthquake
819 physics. Journal of Geophysical Research: Solid Earth, 112(B10).

820 Rudnicki, J. W., & Rice, J. R. (1975). Conditions for the localization of deformation in
821 pressure-sensitive dilatant materials. Journal of the Mechanics and Physics of Solids, 23(6),
822 371-394.

823 Satoh, T., Shivakumar, K., Nishizawa, O., & Kusunose, K. (1996). Precursory localization
824 and development of microfractures along the ultimate fracture plane in amphibolite under
825 triaxial creep. Geophysical Research Letters, 23(8), 865-868.

826 Sylvester, A. G. (1988). Strike-slip faults. Geological Society of America Bulletin, 100(11),
827 1666-1703.

828 Tang, C. A., Liu, H., Lee, P. K. K., Tsui, Y., & Tham, L. (2000). Numerical studies of the
829 influence of microstructure on rock failure in uniaxial compression—part I: effect of
830 heterogeneity. International Journal of Rock Mechanics and Mining Sciences, 37(4), 555-
831 569.

832    Tudisco, E., Andò, E., Cailletaud, R., & Hall, S. A. (2017). TomoWarp2: A local digital
833    volume correlation code. SoftwareX, 6, 267-270.

834    Vasseur, J., Wadsworth, F. B., Lavallée, Y., Bell, A. F., Main, I. G., & Dingwell, D. B.
835    (2015). Heterogeneity: The key to failure forecasting. Scientific Reports, 5(1), 13259.

836    Wang, Y., Allam, A., & Lin, F. C. (2019). Imaging the fault damage zone of the San Jacinto
837    fault near Anza with ambient noise tomography using a dense nodal array. Geophysical
838    Research Letters, 46(22), 12938-12948.

839    Wong, T. F., David, C., & Zhu, W. (1997). The transition from brittle faulting to cataclastic
840    flow in porous sandstones: Mechanical deformation. Journal of Geophysical Research: Solid
841    Earth, 102(B2), 3009-3025.